

Effect of curing methods during a long time gap between two printing sessions on the interlayer bonding of 3D printed cementitious materials

Chen, Yu; Chang, Ze; He, Shan; Copuroglu, Oguzhan; Šavija, Branko; Schlangen, Erik

DOI

[10.1016/j.conbuildmat.2022.127394](https://doi.org/10.1016/j.conbuildmat.2022.127394)

Publication date

2022

Document Version

Final published version

Published in

Construction and Building Materials

Citation (APA)

Chen, Y., Chang, Z., He, S., Copuroglu, O., Šavija, B., & Schlangen, E. (2022). Effect of curing methods during a long time gap between two printing sessions on the interlayer bonding of 3D printed cementitious materials. *Construction and Building Materials*, 332, 1-18. Article 127394. <https://doi.org/10.1016/j.conbuildmat.2022.127394>

Important note

To cite this publication, please use the final published version (if applicable). Please check the document version above.

Copyright

Other than for strictly personal use, it is not permitted to download, forward or distribute the text or part of it, without the consent of the author(s) and/or copyright holder(s), unless the work is under an open content license such as Creative Commons.

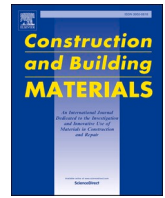
Takedown policy

Please contact us and provide details if you believe this document breaches copyrights. We will remove access to the work immediately and investigate your claim.



Contents lists available at ScienceDirect

Construction and Building Materials

journal homepage: www.elsevier.com/locate/conbuildmat

Effect of curing methods during a long time gap between two printing sessions on the interlayer bonding of 3D printed cementitious materials

Yu Chen, Ze Chang^{*}, Shan He, Oğuzhan Çopuroğlu, Branko Šavija, Erik Schlangen

Microlab, Faculty of Civil Engineering and Geosciences, Delft University of Technology, Delft, The Netherlands

ARTICLE INFO

Keywords:

3D concrete printing
Curing methods
Interlayer bond strength
Long time intervals
Microstructure

ABSTRACT

A good bond between the layers of 3D printed cementitious materials is a prerequisite for having high structural rigidity for the printed elements. However, the influence of printing process on an interlayer bond is still not well understood. This study investigates the influence of curing methods (i.e., air curing, plastic film covering, wet towel covering and water mist-30 min/-60 min) on the interlayer bonding characteristics of 3D printed cementitious materials for a long time interval between two printing sessions. Results showed that the interlayer bonding could be improved by covering the substrate with a plastic film or a wet towel. However, applying water mist every 60 min/30 min on the deposited layer was detrimental to the interlayer bonding. Furthermore, the interlayer bond strength of studied specimens appeared to be dominated by the mechanical strength of the cementitious matrix at the interface rather than its air void structure. Therefore, covering unfinished printed elements with plastic film or wet towels can be a practical solution to maintain a sufficiently humid environment during long waiting periods, which is vital for its interlayer adhesion.

1. Introduction

Extrusion-based 3D concrete printing (3DCP), as the most adopted additive manufacturing technology of concrete, has been widely developed and reported worldwide in the last decade [1-5]. Most 3DCP approaches employ a continuous filament extrusion and layer-wise process for constructing building elements without using formwork [6-8]. Fresh cementitious material is deposited to form sequential layers via a printhead equipped on a digitally controlled robotic arm, gantry or other configurations [1,9,10]. Owing to this sophisticated process, implementing 3DCP in concrete construction can provide many benefits, i.e., saving labor and formwork cost, reducing construction time and waste, improving construction site safety and flexibility of architectural design [6,11-13]. Besides, 3DCP can also be regarded as an environmental-friendly approach to concrete manufacturing using sustainable binders [14-16] and recycled aggregate [17-19].

However, due to the layer-based manufacturing process, the printed component consists of many interfaces that may deteriorate its mechanical properties and durability. According to [9,20], the interlayer bond strength is affected by the thixotropy of printable cementitious materials and the printing parameters. Roussel [21] pointed out that

cementitious materials with high thixotropy can contribute to good buildability and structural build-up but may easily form cold-joint between layers. This phenomenon has been confirmed by extensive studies [22-24]. Moreover, employing a printable mixture but varied printing parameters, i.e., time gaps, nozzle standoff distances, printing speeds and nozzle types, may also result in different interlayer properties [9,22,25,26]. Among these printing parameters, the time interval between two subsequent layers is the most critical factor affecting the bond strength. An inversely proportional relationship between interlayer bond strength and time gap has been reported by many earlier studies [20,22,25-28]. In the literature, the time gap can range from several seconds to 1 h or as long as a few hours to one day. In the case of short time intervals (within 1 h), the amount of air voids formed in the interlayer zone seems to play a dominant role in interlayer bond strength. As reported by [20,22,24,29], increasing the time interval between layers may significantly increase the air void content at the interface. Since the stiffness of the substrate evolves with resting time, for a relatively long time gap (e.g., tens of minutes), the overlay cannot rearrange the orientation of the top surface of the deposited layer resulting in many unfilled areas (wide macropores) between layers [20,22].

^{*} Corresponding author.

E-mail addresses: Y.Chen-6@tudelft.nl (Y. Chen), Z.Chang-1@tudelft.nl (Z. Chang), S.He-2@tudelft.nl (S. He), O.Copuroglu@tudelft.nl (O. Çopuroğlu), B.Savija@tudelft.nl (B. Šavija), Erik.Schlangen@tudelft.nl (E. Schlangen).

<https://doi.org/10.1016/j.conbuildmat.2022.127394>

Received 28 January 2022; Received in revised form 31 March 2022; Accepted 3 April 2022

Available online 8 April 2022

0950-0618/© 2022 The Authors. Published by Elsevier Ltd. This is an open access article under the CC BY-NC license (<http://creativecommons.org/licenses/by-nc/4.0/>).

Table 1
Mix design of printable mixture.

	Type	Content [wt.% of binder]
Binder	PC	40
	LP	20
	CC1	30
	CC2	10
Aggregate	0.125–0.25 mm sand	42
	0.25–0.5 mm sand	78
	0.5–1 mm sand	27
	1–2 mm sand	3
Water	Tap water	30
Admixture	PCEs	2
	HPMC	0.24

A very long time interval between two subsequent layers (from several hours to one day) may not appear in a small printed object, whereas it cannot be avoided for some large-scale printing projects. For example, multiple printing sessions (in each printing session, the time-gap between two layers ranges from several seconds to minutes) may be needed to finish a large-scale building element [9,25]. Due to the temperature increase of the printing setup and other practical issues (e.g., placement of reinforcement), breaks of up to a few hours may be needed between subsequent printing sessions. Note that the long time interval/gap in this paper refers only to the time gap between two

printing sessions. Many earlier studies [25-27,30] have attempted to determine the interlayer bond strength of printed samples with a relatively long time gap. Panda et al. [26] measured the bond strength of printed two-layer samples with 3 h and 6 h of time gaps by conducting uniaxial tension tests. Wolfs et al. [25] employed a tensile splitting test to determine the bond strength of printed specimens with long time intervals, e.g., 4 h, 7 h, and 24 h. Similar works can also be found in [27,30]. In this context, the interlayer bond strength decreases with increasing the time gap and is notably affected by the printing environment. The weak bonding/cold-joint is easily formed by exposing the deposited layer to drying for a long resting time. In contrast, protecting the deposited layer from drying can efficiently retain the moisture of the substrate to improve layer adhesiveness [21,31]. The water loss at an early age can inhibit the strength development at the interface and lead to severe plastic shrinkage [32]. Therefore, applying proper curing on the substrate during the long time interval is essential to improve the bond strength and other mechanical properties of printed cementitious materials. To our knowledge, there has been little study so far about effect of curing methods during a long time gap between layers on the interlayer bonding of printed samples.

The contact area and adhesion between two layers are two critical factors affecting the interlayer bond strength of printed cementitious materials [9,20]. The contact area can be quantified by determining the air void content at the interface. X-ray computed tomography scanning (CT-scanning) coupled with image analysis is the most effectively used technique for indicating the air void features of printed concrete currently [27,29,33-37]. This way, 3D heterogeneity of air void structure can be quantified without making stereological assumptions.

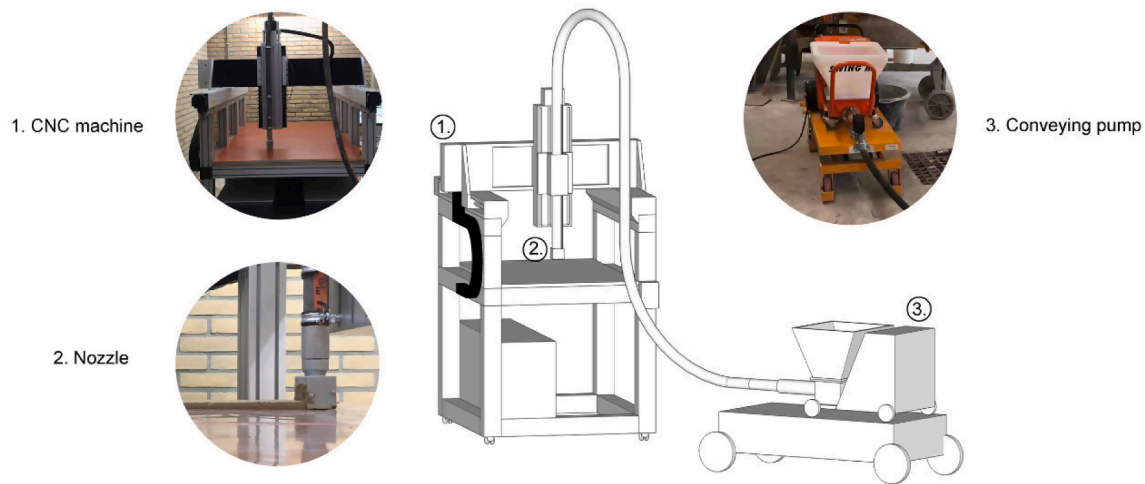


Fig. 1. A lab-scale 3D concrete printing setup at TU Delft, adapted from [20]

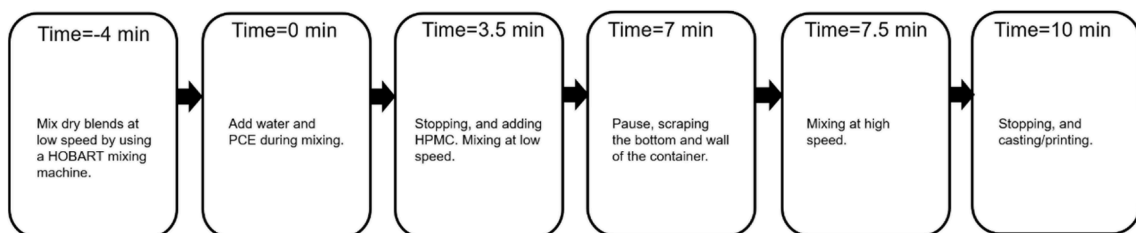
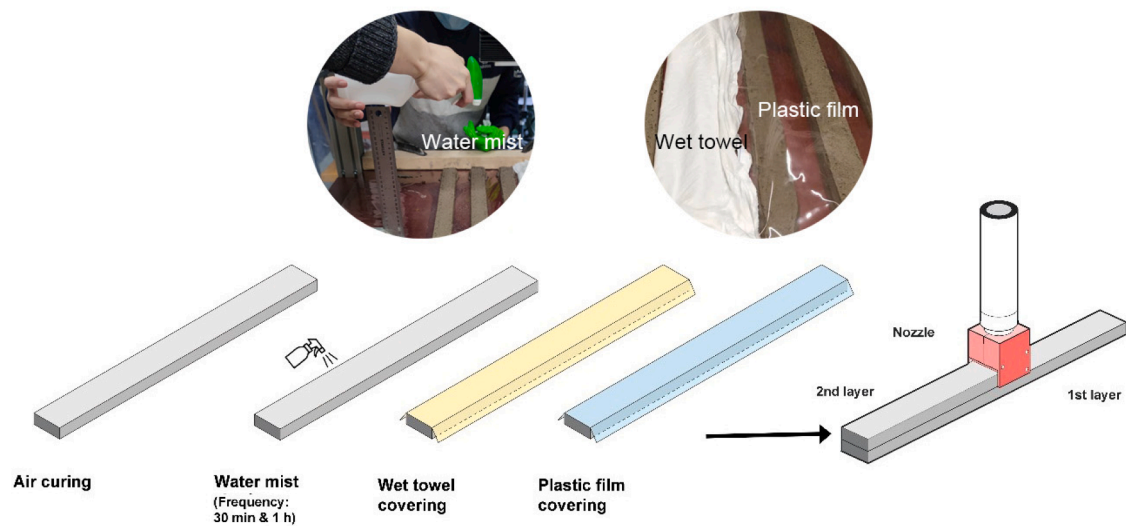


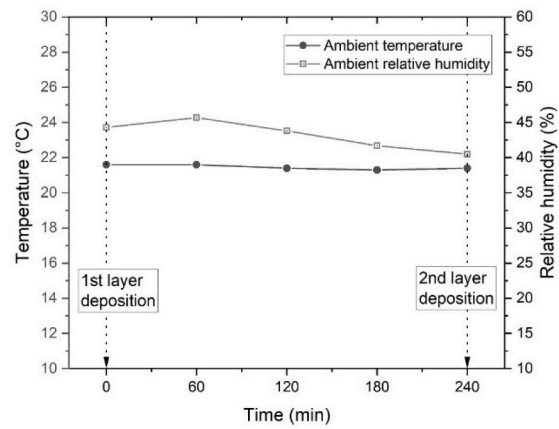
Fig. 2. Illustration of mixing protocol for preparing fresh cementitious materials.



(a)



(b)



(c)

Fig. 3. (a) Schematic diagram of sample preparation by using different curing methods during 4 h of time gap; (b) Printed specimens after the second layer deposition; (c) Ambient temperature and relative humidity during 4 h of time gap.

Table 2
Parameters of 30-min and 60-min frequency water mist samples.

	0	60 min	90 min	120 min	150 min	180 min	240 min
Water mist-30 min	First layer deposition	~7 g per filament	Second layer deposition				
Water mist-60 min	First layer deposition	~7 g per filament	-	~7 g per filament	-	~7 g per filament	Second layer deposition

However, it must be noted that the minimum air void diameter that can be observed using CT-scanning is limited by the machine resolution, being larger for large specimens. Interlayer adhesion in this study refers to the local mechanical strength of the cementitious matrix in the contact area between two layers. However, there is little published data on

the interlayer adhesion of printed cementitious materials. The research to date has focused on air void characterization rather than interlayer adhesion. This is because: (1) In many cases, air void content at the interface dominated the interlayer bonding. The local mechanical strength at the interface might be only slightly modified (or not at all) by

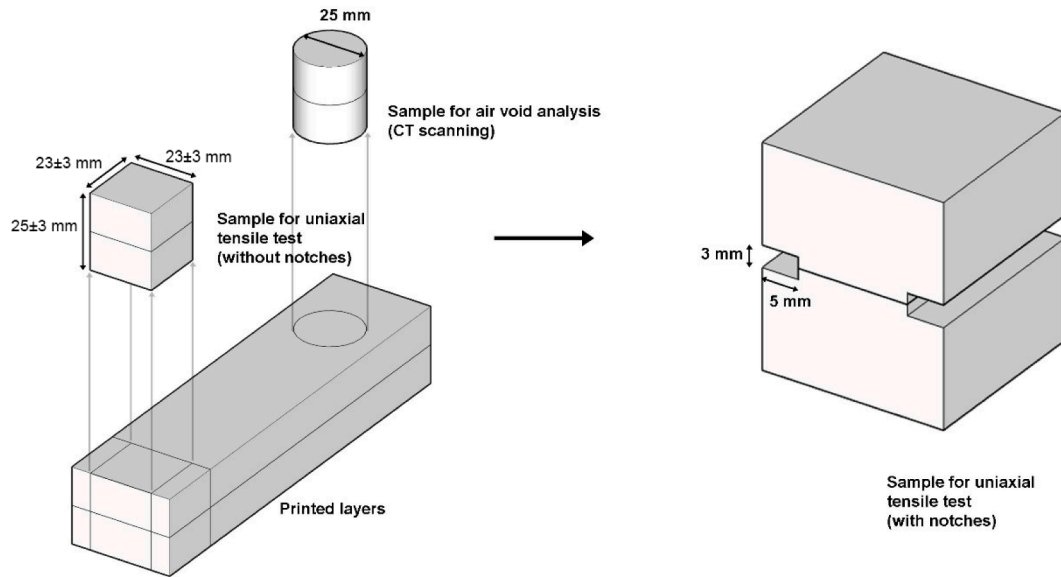


Fig. 4. Left: Extracting cubic and cylindrical specimens from the printed beam; Right: Cubic specimen with notches at the interface for performing the uniaxial tensile test.

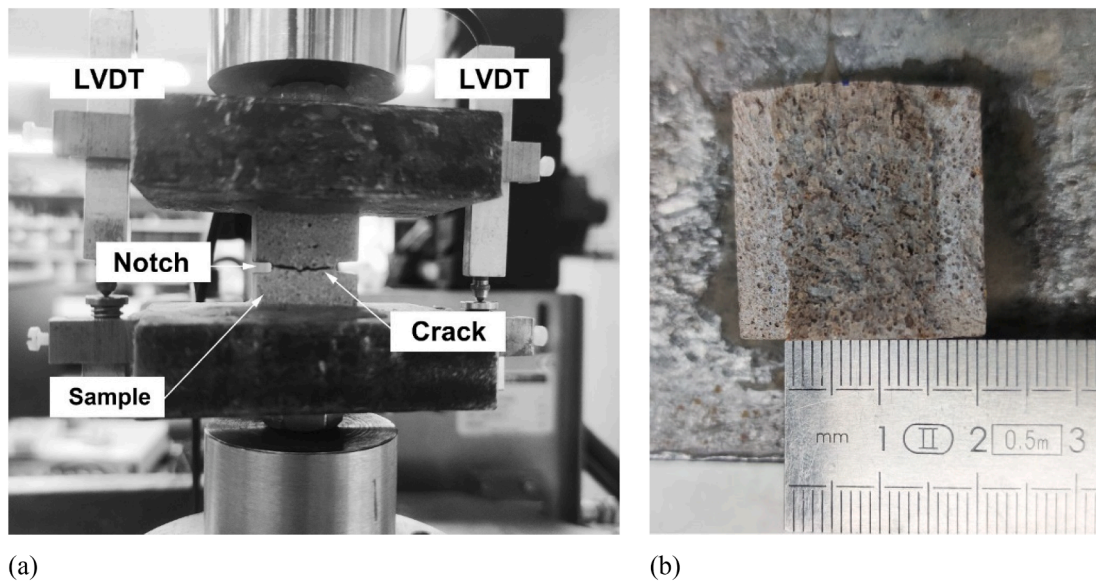


Fig. 5. (a) Uniaxial tensile test setup; (b) Crack surface of the printed specimen.

a short time interval between layers, as reported by [20]. (2) The local mechanical strength of contact area between layers may be influenced by local capillary porosity, micro-cracks, cement hydration degree, and other factors. The mechanism in this context is complicated and underexplored. (3) The current experimental approach may be unable to quantify interlayer adhesion effectively and accurately, especially when large air voids and aggregate particles are also present at the interface. Geng et al. [27] attempted to map the local elastic modulus in the

interlayer zone by performing a series of nano-indentation tests. However, intensive experimental works might be expected by using such a manner.

Overall, instead of experimental tests, employing numerical models to predict the local strength of the cementitious matrix at the interface might be an appropriate way at this stage. As a mechanical modeling approach, the discrete lattice fracture model has been widely utilized to mimic the fracture process of the hardened cementitious materials since

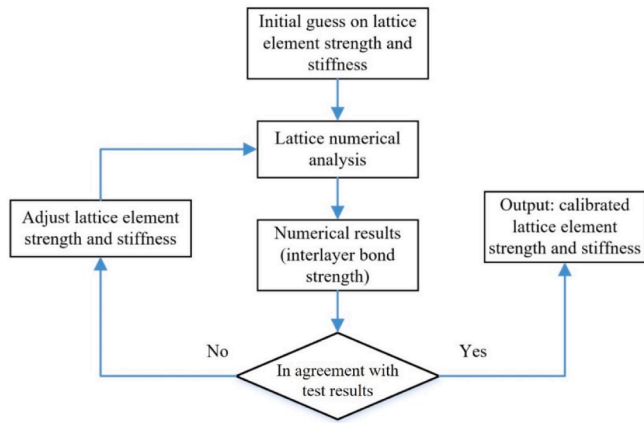


Fig. 6. Flowchart of inverse lattice modeling.

the simulated crack pattern and strength (especially uniaxial tensile strength) are very close to the experimental findings [38-40]. In our earlier study [20], we used a 2D lattice fracture model to simulate the uniaxial tensile test of different printed samples with short time intervals between layers (e.g., 20 s, 1 min and 10 min). The digital material structure was acquired by CT scanning. The predicted bond strength from the lattice model corresponded very well with the test result. On the basis of digital structure and mechanical behaviors of cementitious materials, it is also possible to compute the local mechanical strength through an inverse modeling process. Herein, we propose applying inverse 2D lattice fracture modeling to predict the local mechanical strength of cementitious matrix in the interlayer zone.

The goal of this paper is to systematically investigate the impact of different curing methods during a long time gap on the interlayer bond strength and microstructure of 3D printed cementitious materials. For determining the interlayer bond strength, the printed 2-layer samples were tested in the uniaxial tension under fixed boundary conditions. Moreover, the digital material structure was acquired by using CT scanning. Based on the reconstructed 3D volume, air void features of various printed specimens, including content, size, and distribution, can be determined and compared. Furthermore, an inverse 2D lattice model was employed to quantify the local mechanical strength of cementitious matrix in the interlayer zone of different printed specimens. Finally, the microstructure of the interlayer zone was also observed under an environmental scanning electron microscope (ESEM).

2. Materials and methods

2.1. Raw materials and mix design

The printable mixture used in this work was introduced in our earlier studies [20,41]. Primary cementitious materials were CEM I 52.5R Portland cement (PC), limestone powder (LP), low-grade calcined clay (CC1), and high-grade calcined clay (CC2). CC1 that contains about 50 wt% of metakaolin was provided by Argeco, France. CC2 with nearly 95 wt% of metakaolin was supplied by Burgess, USA. As shown in Table 1, the binder comprised 40 wt% of PC, 20 wt% of LP, 30 wt% of CC1, and 10 wt% of CC2. Quartz sand (grain size in the range of 0.125–2 mm) was employed as aggregate. The aggregate-to-binder ratio and water-to-binder ratio were 1.5 and 0.3, respectively. Additionally, 2 wt% polycarboxylate ether superplasticizer (PCEs) and 0.24 wt% hydroxypropyl methylcellulose (HPMC) were added to ensure sufficient buildability. According to [41], the initial setting time of the studied mixture is about 80 min.

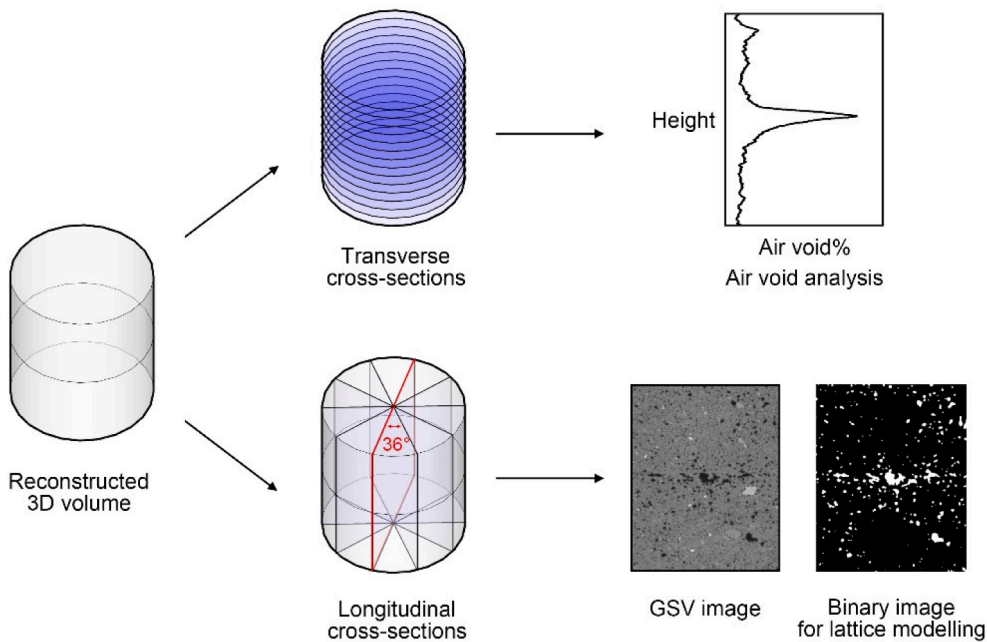


Fig. 7. Illustration of transverse cross-sections for air void analysis and extracted longitudinal cross-sections for 2D lattice modeling.

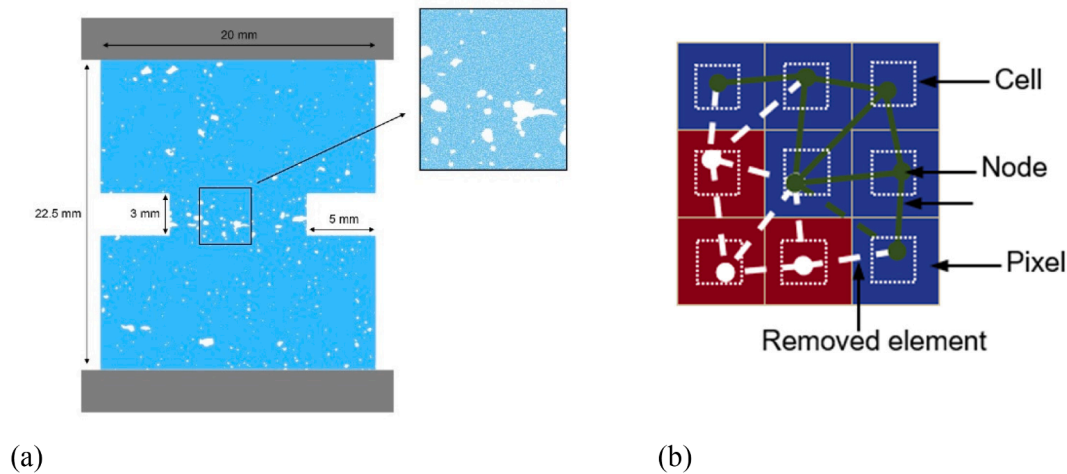


Fig. 8. Illustration of lattice model generation: (a) The construction of 2D lattice network; (b) An example of the overlay procedure for 2D lattice mesh (red-air voids, blue-solid phases), adapted from [20]

2.2. Sample preparation

The printed specimens were manufactured using the lab-scale 3DCP setup of TU Delft. As introduced in our earlier works [11,20], the 3DCP configuration comprises a 3D freedom Computer Numerical Control (CNC) machine, a PFT Swing M conveying (progressive-cavity) pump, and a hybrid back- and down-flow nozzle with a rectangular opening of $40 \times 15 \text{ mm}^2$ (see Fig. 1). In addition, a material hose with 25 mm inner diameter and 5 m length was used to connect the nozzle and the pump. About 18 L of the fresh mixture was prepared for each batch according to the specific mixing protocol as described in Fig. 2.

In this study, the material flow rate was predefined as 1.6 L/min with respect to a nozzle moving speed of 45 mm/s. The nozzle standoff distance was kept as 0 mm in all test series. All printed beams (800 mm in length, 40–42 mm in width, and 26–30 mm in height) contained two layers, and there was only one filament for each layer. After the deposition of the first layer, four different curing methods, i.e., air curing, water mist, wet towel covering (the moisture contents of wet towel: $50.8 \pm 0.5\%$), and plastic film covering (thickness of plastic film: 36 μm), were applied during 4 h time interval. Compared with plastic film, covering the fresh sample with a wet towel helps maintain a slightly higher surface moisture content. Then, a new batch of the fresh mixture was prepared for printing the second layer (see Fig. 3(a and b)). There are two frequencies (30 min and 1 h) for the curing method of spraying water mist. The specific parameters are given in Table 2. About 7 g of water was sprayed per filament each time. Fig. 3(c) illustrates that the ambient temperature and relative humidity (RH) during the 4 h of time gap stabilized at 23–25 $^{\circ}\text{C}$ and 38% RH. Mold-cast samples ($160 \times 40 \times 40 \text{ mm}^3$) were prepared using extruded materials and tested to compare the interlayer bonding and air void content of printed specimens. Freshly prepared mortar was filled in expanded polystyrene foam mold, and compaction was applied manually to reduce the air void content. All samples were cured under the plastic film at ambient temperature and RH for the first day. After that, the samples were stored in a fog room (20 \pm 2 $^{\circ}\text{C}$, and 99% RH) before cutting and testing.

2.3. Uniaxial tension test

As shown in Fig. 4, prismatic specimens with $25 \pm 3 \text{ mm}$ height and $23 \pm 3 \text{ mm}$ side length were sawn from cured samples at 27 days. A notch (3 mm height and 5 mm depth) was sawn on the two sides of the samples at the interface area (at the same position for cast samples) to

ensure samples failed at the interface. Fig. 5 illustrates the uniaxial tensile test setup built on a servo-hydraulic Instron 8872 machine. To keep the same deformation along the four sides of the specimen, the prepared specimen was glued between two non-rotating platens. The deformation was controlled by the average value of two linear variable differential transducers (LVDTs), and the loading rate was kept as 0.01 $\mu\text{m/s}$ constantly. For each parameter, three repetitions were executed.

2.4. X-ray computed tomography

The grayscale-based digital microstructure of each specimen was acquired using X-ray computed tomography scanning (CT scanning). The obtained grayscale value (GSV) images were employed to characterize the air void characteristics of printed and cast specimens. Cylindrical samples with 25 mm diameter and $25 \pm 3 \text{ mm}$ height were extracted from samples as explained in the Section 2.2 at the material age of 28 days. A Phoenix Nanotom Micro CT-Scanner was used, and 1441 tomographic images were acquired on a digital GE DXR detector under 120 kV/60 IA of the X-ray source. A spatial resolution of $25 \times 25 \times 25 \mu\text{m}^3/\text{voxel}$ was obtained. By using the software Phoenix Datos|x Reconstruction 2.0, the 3D tomographic reconstruction has been conducted. For each specimen, about 900 transverse cross-sections (800 slices for the cast sample) of GSV images were extracted for performing air void analysis (see Fig. 7). The thresholding method was used to segment cementitious material and air void in GSV images based on ImageJ software. Note that only the air voids larger than 25 μm (image resolution) were detected.

2.5. Inverse lattice modeling

In the current study, the lattice fracture model was utilized to study the impact of air voids on interlayer bond strength and calibrate the local strength of cementitious matrix in the interlayer zone. The grayscale-based digital microstructure is first employed to build the numerical model for the uniaxial tensile test. The local mechanical property (i.e., tensile strength) of lattice elements at the interface can then be derived through inverse lattice modeling. The detailed procedure can be found in Fig. 6.

If the main crack is formed at the interface area (where we also made notches) in the uniaxial tensile test, we assumed that the tensile strength of printed samples is equal to the tensile strength of the interlayer zone, which is only determined by the air void structure and/or local tensile

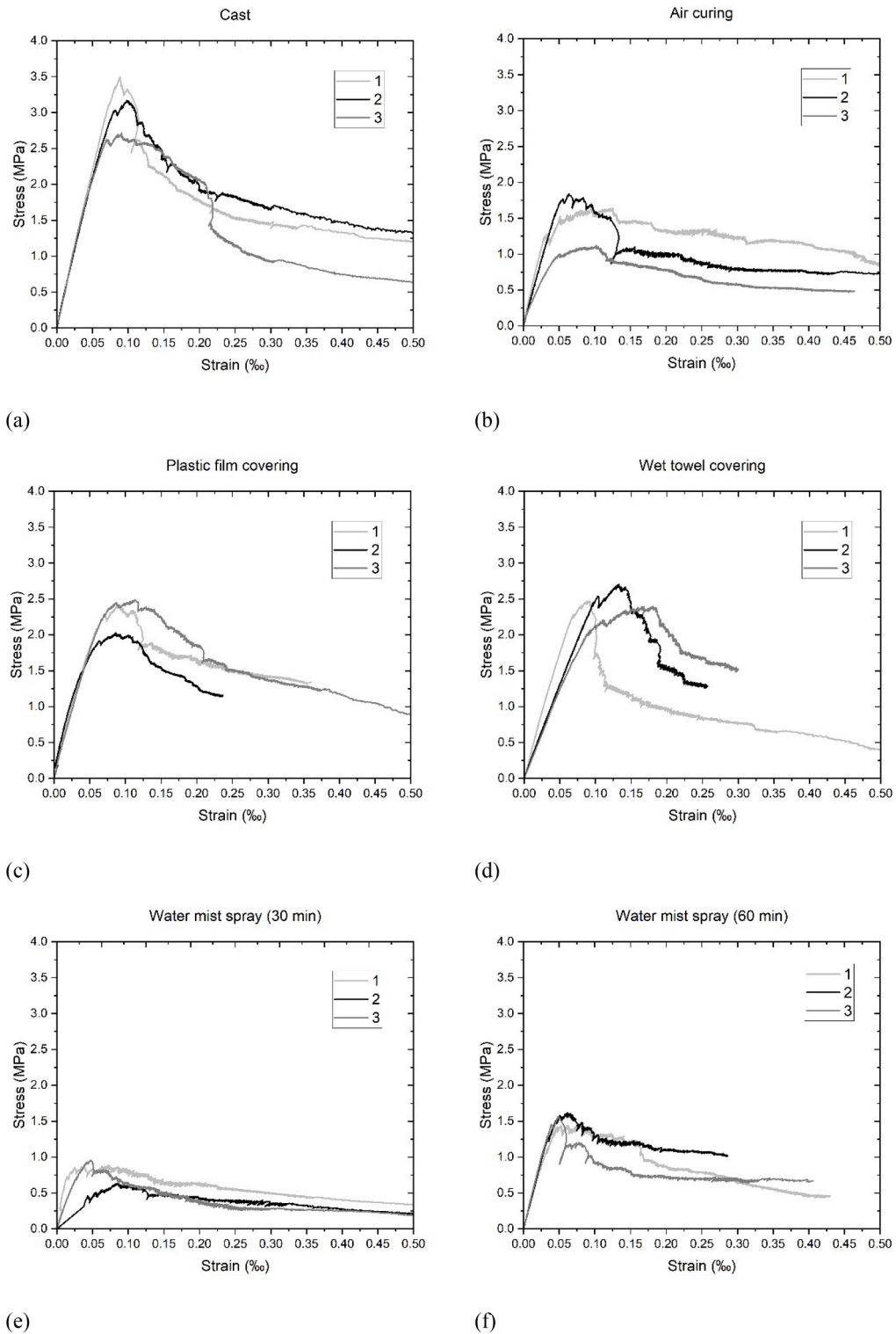


Fig. 9. Stress and strain curves of uniaxial tensile tests at 28 days. (a) Cast; (b) Air curing; (c) Plastic film covering; (d) Wet towel covering; (e) Water mist-30 min; (f) Water mist-60 min.

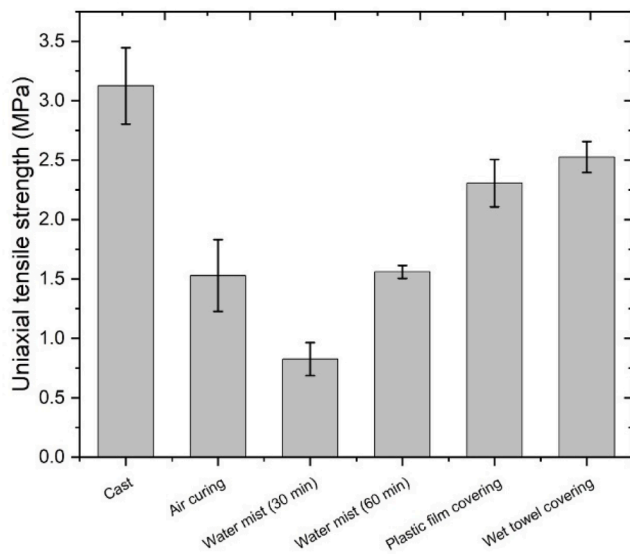


Fig. 10. The interlayer bond strength of different samples at 28 days.

strength of cementitious matrix in the interlayer zone.

The 2D lattice model adopts a network of Timoshenko beams with linear elastic behavior to discretize the material domain. The heterogeneity of the network was achieved by overlapping the digital material structure (i.e., a digital material structure obtained by CT scanning [42]) on the lattice and assigning different local mechanical properties to the elements based on their positions [43]. The numerical model was subjected to external loading and boundary conditions. A series of linear analyses were performed to simulate the fracture process. Once the beam stress reaches the fracture criterion, this element was removed from the system to mimic crack propagation [20,43]. In this study, several longitudinal cross-sections were extracted from the 3D reconstructed volume, as shown in Fig. 7. These GSV images were then transferred to binary images which consist of two phases, i.e., pore and solid phases. For each printed sample, five 2D binary images with 22.5 mm in height and 20 mm in width (900×800 pixels) were extracted at every 36-degree along with the axis of the cylinder sample, as shown in Fig. 7. These binary images were utilized to build the lattice models. Two notches (3 mm in height and 5 mm in width) were created in the mid-height of the mesh, as shown in Fig. 8(a).

The network of lattice model (see Fig. 8(a)) can be generated as follows [44]. (1) The material domain was divided into a grid of square cells. (2) A sub-cell was created in the center of cell, and a node was placed randomly in each sub-cell. Note that the ratio between the length of the cell and the sub-cell was selected as 0.5, which can introduce the geometry disorder in the digital material structure without creating significant differences in the length of elements [45]. (3) Delaunay triangulation was then conducted on the set of the defined nodes, wherein nodes in adjacent Voronoi cells were connected with beam elements. Consequently, the Poisson's ratio of such a mesh configuration is 0.18 [46], which is appropriate for cementitious materials [47].

As shown in Fig. 8(b), solid (i.e., the cementitious matrix) and air voids were considered in the 2D material structure. During the lattice mesh generation, the lattice beam was removed if one node was located in the void area. All the lattice elements found in the solid phase of the interlayer zone were assigned the same linear-elastic-brittle constitutive law (tensile strength and elastic modulus). According to Ref [45], the local compressive strength is not needed for simulating fracture behavior of such material under uniaxial tension. Lattice elements except for interlayer were set to the same elastic modulus while no element failure was defined among them. This operation can eliminate the impact of non-interlayer on the calibration of local strength of matrix

at the interface. The computational uniaxial tensile tests were performed by uniformly applying nodal displacement on one side and fixing any degrees of freedom of the nodes on the opposite side.

2.6. Microstructural observations

The specimens with 10–15 mm thickness were sawn from the printed beam. Before polishing, the extracted specimens were impregnated using low-viscosity epoxy. The studied surface of each sample was then ground employing silicon carbide abrasive papers and polished using 6, 3, 1 and 0.25 μm diamond pastes. Lab-grade ethanol was employed as a coolant for grinding and polishing. Finally, the microstructure of the interface area in the polished section was observed by backscattered electrons (BSE) mode on an environmental scanning electron microscope (ESEM).

3. Results and discussion

3.1. Interlayer bond strength

Fig. 9 illustrates all stress and strain curves of uniaxial tensile tests using various samples with different parameters. It can be found that all curves displayed a similar pattern. Before reaching the peak value, the stress increased quasi-linearly with the increase of deformation. For most specimens, the peak stress appeared at the strain of 0.08–0.2 %. However, the samples with water mist-30 min/-60 min corresponded to a small deformation (0.04–0.12 %). After the peak, the stress decreased with increasing deformation. Finally, the main crack was formed at the interface area (the area containing two notches) of each specimen. The peak value of each curve in Fig. 9 was collected and regarded as the uniaxial tensile strength. As shown in Fig. 10, the cast sample displayed higher tensile strength than the printed samples. Compared to the air cured specimens, employing plastic film covering and wet towel covering during 4 h time gap can significantly improve the interlayer bonding. An increase in uniaxial tensile strength of about 51% and 65% were observed in the samples with plastic film covering and wet towel covering, respectively. Both conditions can decrease the water evaporation rate, thereby enhancing interlayer bond strength [21,31]. In addition, covering a wet towel can slightly increase the surface moisture of the substrate in contrast to plastic film (see Fig. A1. Appendix A), which may result in slightly higher bond strength. Note that the increase in interlayer bond strength can be negligible if the standard deviation is considered. Nevertheless, applying water mist per 30 min/60 min showed minor improvement or adverse effects. The bond strength was reduced by nearly 50% when using water mist per 30 min. It seems that the “too wet” surface caused by water mist weakened the interlayer bonding, which is in agreement with the findings of Sanjayan et al. [48]. The possible reasons are discussed in Section 3.4.

3.2. Air void analysis

Fig. 11(a) compares the local porosity (referred to the cumulative air void content of each transverse GSV image) along with the sample height of different studied specimens. It can be observed that the printed samples exhibited a much higher local porosity at the interface compared to the printed layer zones. In contrast, the air voids were evenly distributed from the bottom to the top of the cast sample. The maximum local porosity of each printed sample was plotted in Fig. 11 (c). The maximum value appeared at the interface area for the printed specimen. However, the magnitude difference is relatively small among printed samples.

On the other hand, it might be difficult to describe the air void distribution of printed specimens only relying on the local porosity. The high local porosity may be attributed to numerous small air voids or only several large air voids at the same sample height. To figure out that, the average air void diameter of each transverse GSV image (determined by

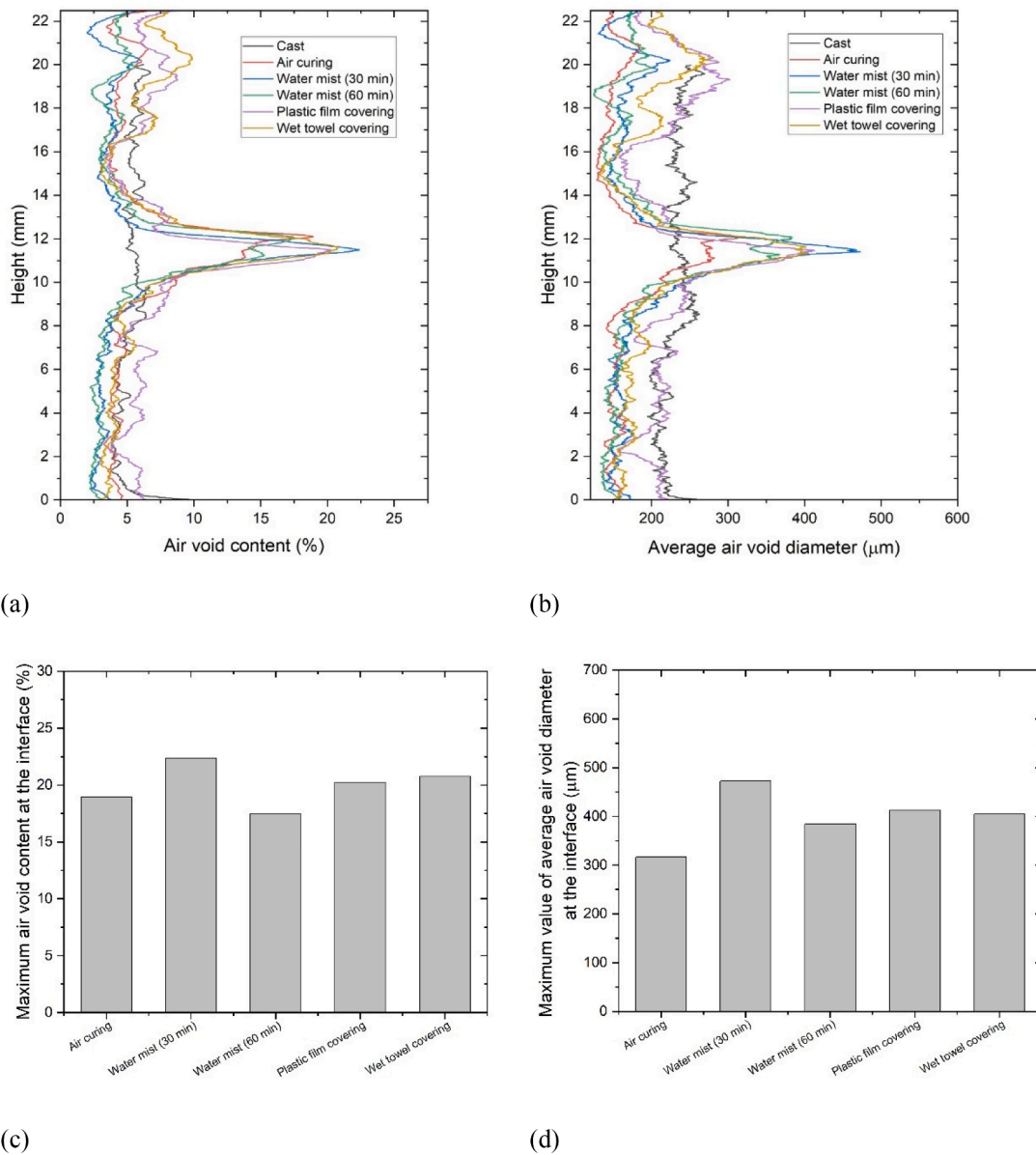


Fig. 11. (a) Local porosity VS. sample height of specimens with different curing methods; (b) Average pore diameter VS. sample height of specimens with different curing methods; (c) The maximum local air void content of different samples; (d) The maximum value of average air void diameter of different samples.

Analyze Particles, ImageJ software) along with sample height was illustrated in Fig. 11(b). A similar curve pattern has been inspected between Fig. 11(a and b). Fig. 11(d) presents the maximum average air void diameter of different samples. A high local porosity corresponded to a high average air void diameter except for the samples with air curing and wet towel covering. In addition, for each studied specimen, the diameter and position of every air void (determined by 3D Objects Counter, ImageJ software) in the interlayer zone (sample height: 10–13 mm in Fig. 11(a)) is presented in Fig. 12. Many large air voids were clearly found at the interface area of printed specimens. This confirms that the high local porosity and average pore diameter at the interface are ascribed to the presence of large air voids. However, the samples with plastic film and wet towel curing displayed a comparable amount of large air voids to the sample with water mist-30 min. Therefore, the findings based on the air void quantification cannot clearly explain the test results of interlayer bond strength. Air voids ($>25 \mu\text{m}$) at the interface appeared to not play the dominant role in influencing the interlayer bond strength for printed specimens in this study.

3.3. Local strength of matrix at the interface

Except for the air void content, the adhesion between two subsequent layers is another critical factor influencing the interlayer bond strength. The interlayer adhesion can be understood as the local mechanical strength of the cementitious matrix in the interlayer zone. For each specimen, five simulations were conducted on the basis of 2D longitudinal slices extracted from different locations in Fig. 7. The simulated global tensile stress VS. strain curves and crack patterns of different printed samples were presented in Fig. 13 (see Fig. A2, Appendix A) and Fig. 14 (see Fig. A3, Appendix A). The fracture pattern of simulated specimens showed a tendency for cracks to propagate along the macropores. In addition, a brittle behavior is observed in the simulation since the constitutive relation of all lattice elements (localized at interlayer zone) for each specimen were assigned as elastic-brittle. Furthermore, due to the 2D model, the crack cannot propagate out of plane, resulting in the linear-brittle behavior [20].

Fig. 15(a) compares the local tensile strength of lattice elements in the interlayer zone of different printed specimens. It can be found that

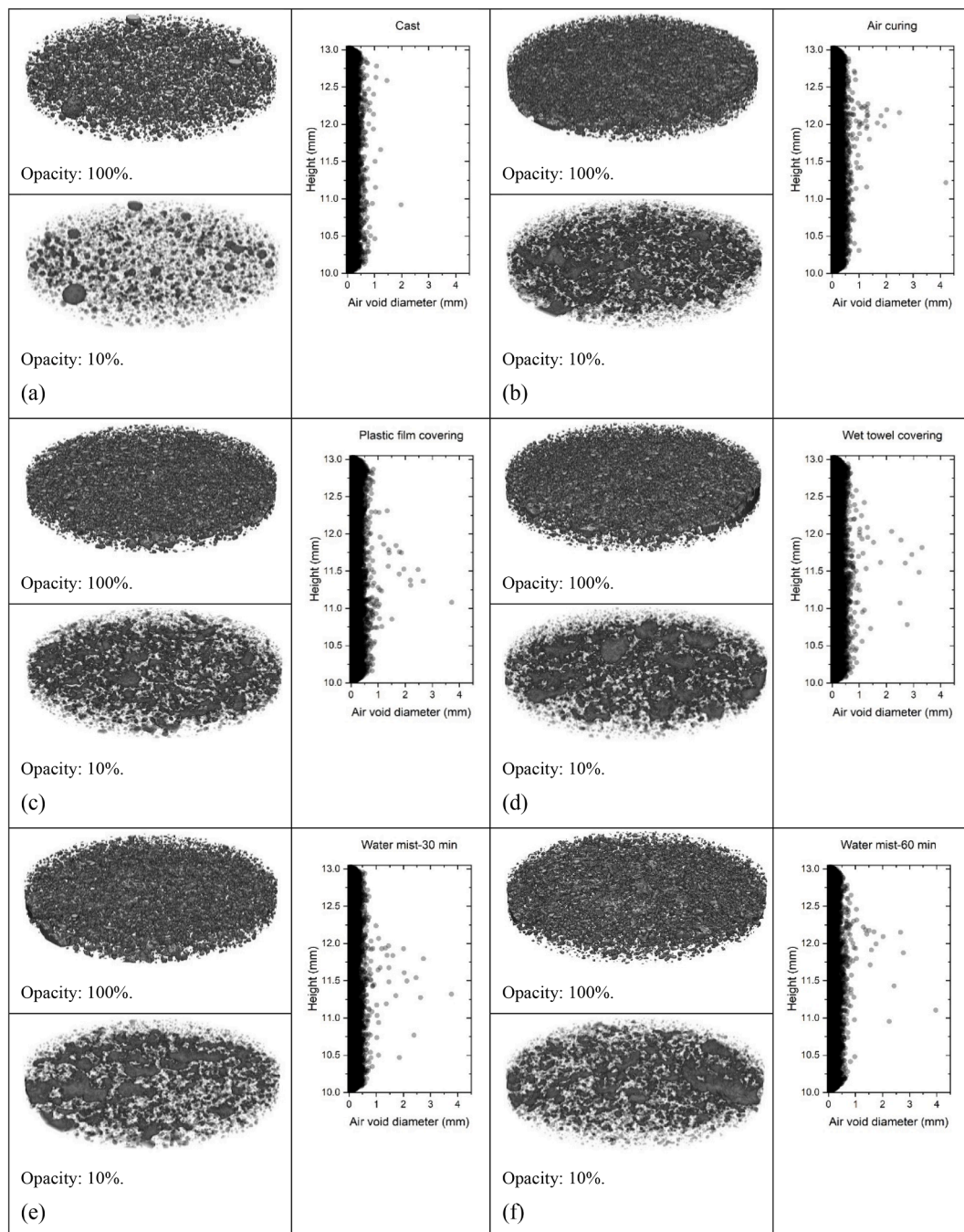


Fig. 12. 3D visualization of air voids (left) and the air void diameter VS. sample height in the interlayer zone (right). (a) Cast; (b) Air curing; (c) Plastic film covering; (d) Wet towel covering; (e) Water mist-30 min; (f) Water mist-60 min.

the sample prepared using water mist-30 min displayed the lowest local tensile strength. In contrast, the obtained lattice element of the sample with water mist-60 min showed comparable local tensile strength to the sample with air curing, whereas much higher values were obtained by samples with plastic film and wet towel covering. Furthermore, a linear relationship between the simulated local tensile strength of lattice element and tensile strength of the printed specimen was demonstrated in Fig. 15(b). The R-squared value of the fitted curve was about 0.96, which appeared to confirm the dominant role of local mechanical performance of matrix in the interlayer zone on interlayer bonding of printed specimen in this work. However, a micromechanical test based on, e.g., nano-indentation (see [27]) may be required to validate the simulated local mechanical performance of the matrix in the interlayer

zone in further investigation.

3.4. Influences of different curing methods during 4 h on the microstructure at the interface

Instead of observing the air voids, the contact area/interface between two layers was emphasized in the microstructural observation under ESEM. Fig. 16 illustrates the typical interlayer zone of printed samples with plastic film covering, wet towel covering, and air curing. The contact area between two layers in these samples showed very similar features, i.e., porous matrix structure and many micro-cracks, which can weaken the matrix locally [27]. It is worth noting that small air voids (<25 μm) and capillary pores in the contact area in

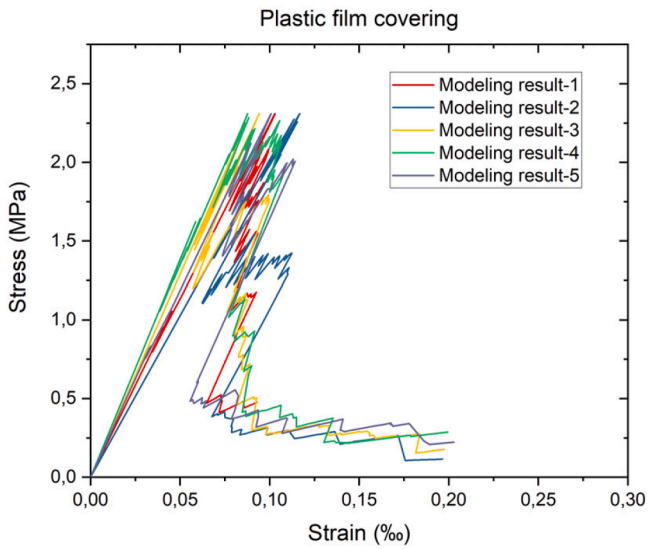


Fig. 13. The simulated stress and strain curves of the printed specimen with plastic film covering.

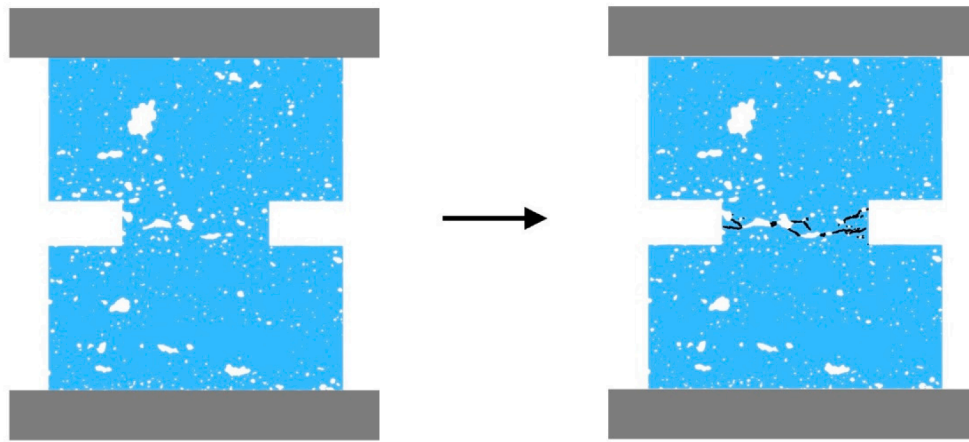


Fig. 14. The simulated crack patterns of the printed specimen with plastic film covering at fracture stage (left: initial specimen; right: fractured specimen). White area-air voids; Black area-cracks; Blue area-cementitious materials.

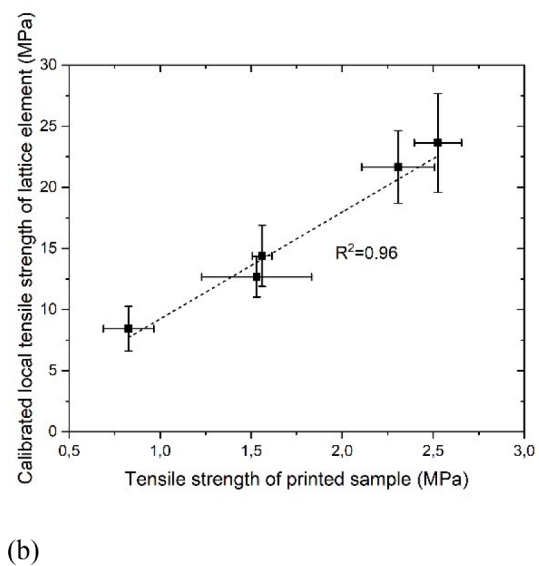
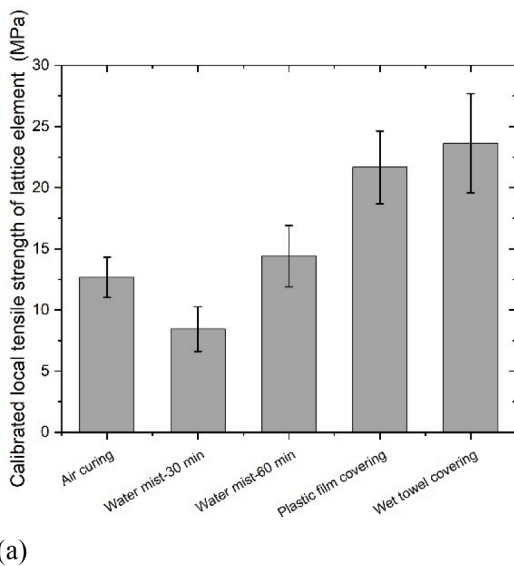


Fig. 15. (a) The calibrated local tensile strength of lattice element in the interlayer zone in the simulations for the different printed specimens; (b) The correlation between the calibrated local tensile strength of lattice element and the tensile strength obtained by the uniaxial tensile test.

Fig. 16(b, d and f) could not be detected by CT scanning in this study.

According to Keita et al. [31], protecting the 1st layer (cast mortar) from drying during a long resting time (up to 24 h) before casting the second layer can help significantly in retaining the bond strength. The authors pointed out that the decrease of relative interlayer bond strength may be only significant once the internal water flow induced by the capillary gradient cannot balance the water loss of the layer surface during drying. Consequently, a dry area with high capillary porosity is formed in the substrate. After the second layer deposition, air-filled pores and voids in the dry regions of the substrate tend to release air for absorbing water. The released air stays entrapped at the interface due to the relatively high viscosity of the deposited material [26,49,50]. On the other hand, if the water retention property of the fresh mixture is too high (due to the addition of HPMC [51]) or other reasons related to capillary gradient, the water from the second layer may have difficulty moving into the air-filled pores and voids of the substrate. As a result, dry zones with high porosity in the first layer will be retained (see [31]). Additionally, the micro-cracks caused by plastic/drying shrinkage are critical for printable mortar within the first 4 h after extrusion [47,48], which also seems to be governed by surface drying [52]. In this study, the water evaporation rate appeared to be diminished by covering the layer surface with a plastic film or a wet towel. The quantities of small air voids, capillary pores and micro-cracks in the interlayer zone may be

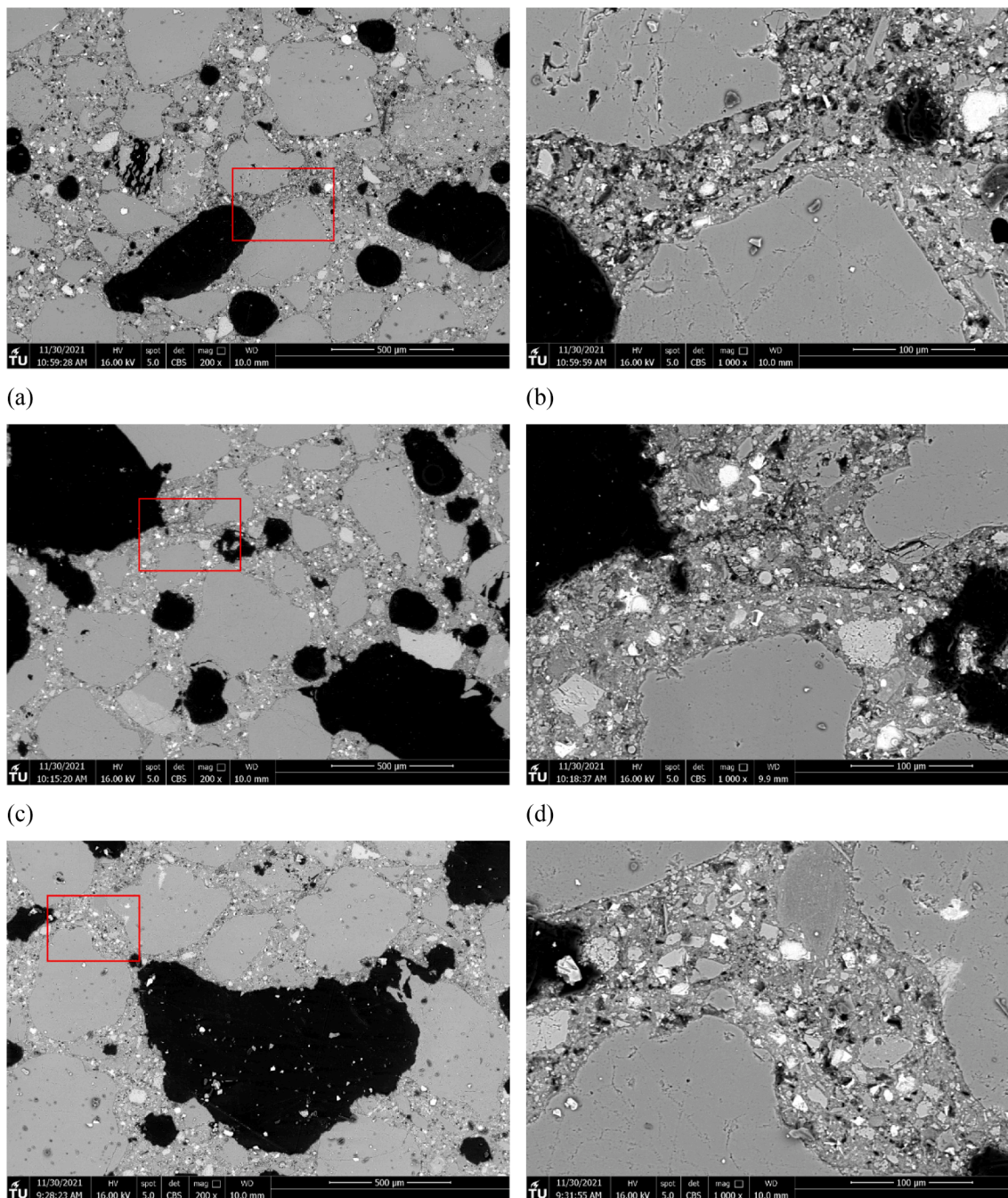


Fig. 16. BSE micrographs of the typical interlayer zones in the printed specimens: (a) Plastic film covering, magnification of $\times 200$; (b) Interface details in (a), magnification of $\times 1000$; (c) Wet towel covering, magnification of $\times 200$; (d) Interface details in (c), magnification of $\times 1000$; (e) Air curing, magnification of $\times 200$; (f) Interface details in (e), magnification of $\times 1000$.

therefore reduced. However, these are not evidently quantified by the current work. To confirm this hypothesis, a quantitative microstructure analysis in terms of small air voids ($< 25 \mu\text{m}$), capillary pores and microcracks characterization in the interlayer zone should be conducted in further investigation.

Compared with printed specimens mentioned above, the interlayer zone of printed samples with water mist-30 min/60 min exhibited different metrics. As shown in Fig. 17, a light-gray strip was visible at the interface, which indicates the boundaries of two layers. To slow down the water evaporation rate and compensate for water loss, water mist was applied on the surface of the deposited layer during the resting time with a specific frequency (30 min or 60 min per time). However, the

excess water droplets remained at the interface even after the second layer was deposited, which created an environment for promoting portlandite precipitation. Consequently, portlandite and/or calcite were formed at the interface (Fig. 18). The presence of the portlandite and/or calcite layer can rarely contribute to the strength of the matrix [53,54]. Still, it may inhibit the interaction and formation of C-S-H gel localized at the contact area resulting in an extremely weak local bonding. The portlandite and/or calcite layer at the interface of the printed specimen with water mist-30 min is thicker than that of the printed specimen with water mist-60 min since more amount of water has been applied during the resting time. Also, more quantities of such thick layers can be expected in the interlayer zone of the printed specimen with water mist-30

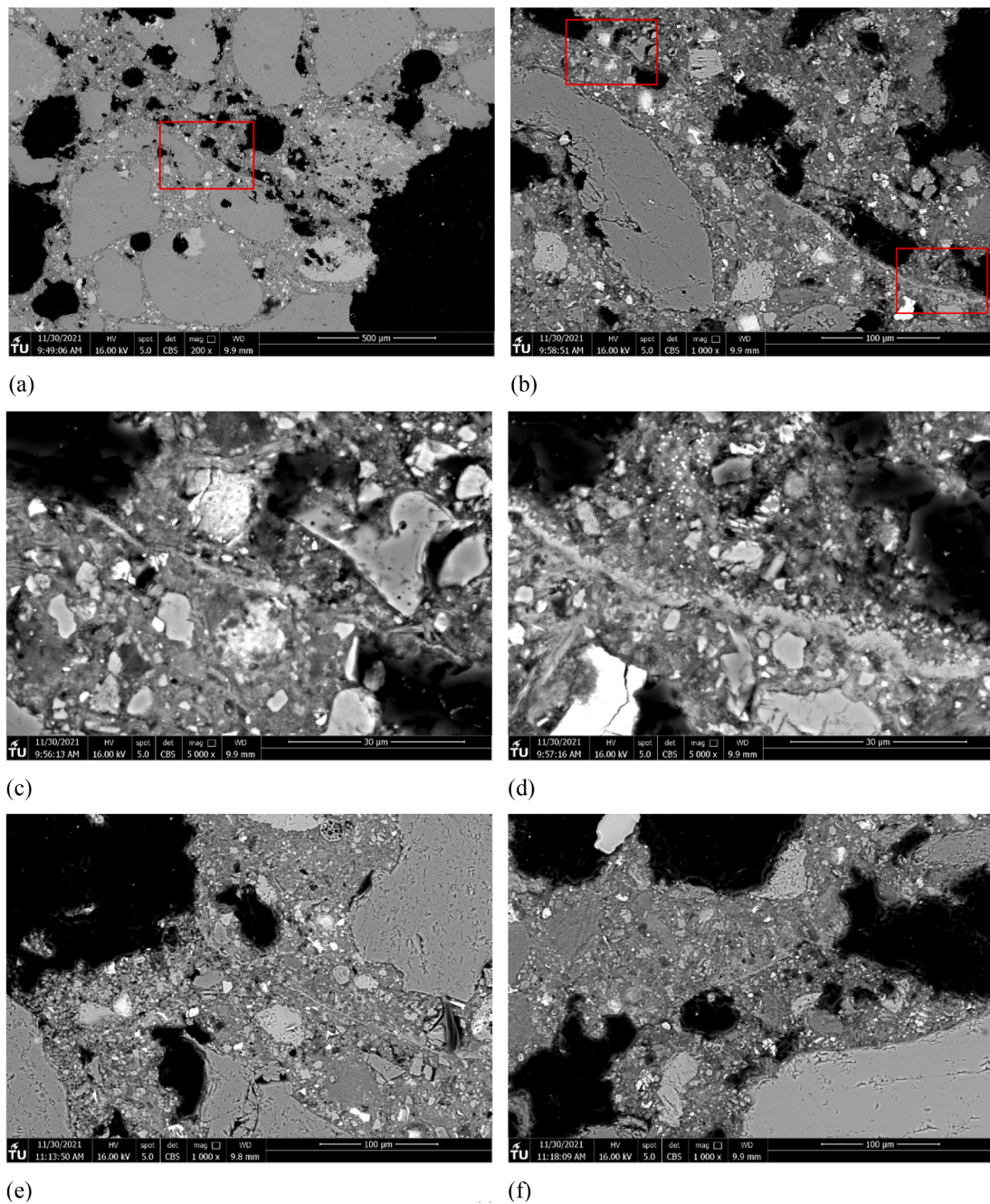


Fig. 17. BSE micrographs of the typical interlayer zones in the printed specimens: (a) Water mist-30 min, magnification of $\times 200$; (b) Interface details in (a), magnification of $\times 1000$; (c) Interface details-portlandite and/or calcite layer (light-gray strip) in (b) Left, magnification of $\times 5000$; (d) Interface details-portlandite and/or calcite layer (light-gray strip) in (b) Right, magnification of $\times 5000$; (e) (f) Interface details of water mist-60 min, magnification of $\times 1000$.

min, which eventually leads to the weaker interlayer bond strength. Additionally, the water droplets that remained at the interface zone seemed to increase the local water to cement ratio (w/c). The increased local w/c leads to higher capillary porosity [47] (portlandite crystals can find space to grow [33,55,56]), which can further dilute the matrix density at the interface, thereby weakening the local mechanical performance.

4. Conclusions

The present study was designed to determine the influence of different curing methods, i.e., air curing, plastic film covering, wet towel covering, water mist-30 min and -60 min, during 4 h time gap on the

interlayer bond strength of 3D printed cementitious materials. The main findings were summarized as follows.

- The interlayer bond strength was significantly enhanced by covering the resting layer with plastic film or wet towel for 4 h between layers compared to exposing the resting layer under ambient environment. However, applying water mist every 60 min or 30 min cannot improve or negatively affect the interlayer bond. Bond strength was reduced by nearly 50% using water mist per 30 min.
- Compared to the cast sample, the printed samples with a 4 h time gap displayed much higher local air void content and average air void diameter at the interface (induced by more quantities of large air voids in the interlayer zone), which may govern the lower uniaxial

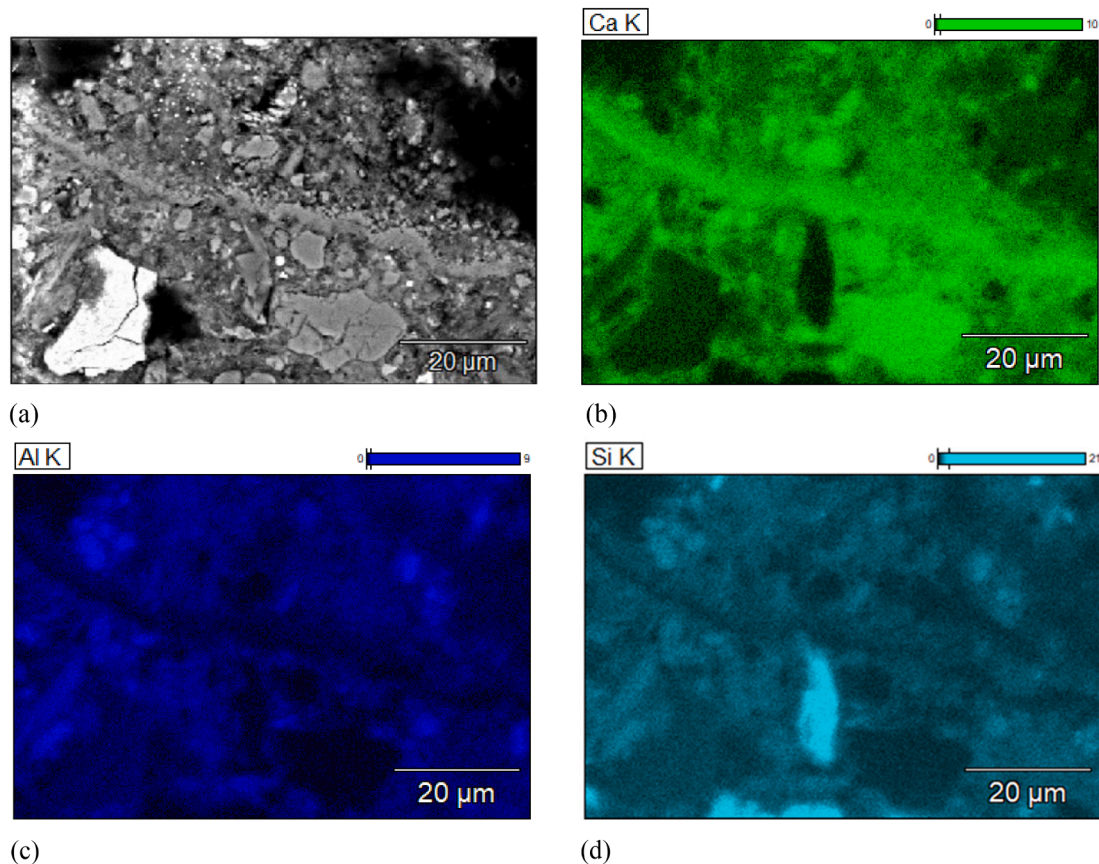


Fig. 18. (a) BSE micrograph of the typical interlayer zones in the printed specimen (Water mist-30 min); (b) Scanning electron microscopy coupled with energy dispersive spectrometry (SEM-EDS) elemental mapping image – Ca (calcium); (c) SEM-EDS elemental mapping image – Al (aluminum); (d) SEM-EDS elemental mapping image – Si (silicon). Portlandite and/or calcite appear to be the main phases in the light-gray strip between the two layers.

tensile strength. However, the magnitude difference of the above-mentioned air void characteristics is relatively small among different printed specimens.

- For printed specimens with a 4 h time gap, the local mechanical strength of the cementitious matrix in the interlayer zone appeared to play a dominant role in interlayer bond strength. The local tensile strength of the lattice element in the interlayer zone can be determined by using inverse 2D lattice modeling. The printed specimen with a high uniaxial tensile strength exhibited a high simulated local tensile strength of the lattice element. Micromechanical testing (e.g., nano-indentation test) is required for further validation.
- Covering or sealing the deposited layer by plastic film or wet towel is recommended as an applicable approach for improving interlayer bond strength with a long time interval. Both methods can slow down the material drying during the resting time, which may eventually decrease the small air void (<25 μm) content, capillary porosity, and micro-cracks localized at the contact area between layers. However, validation regarding the quantification of small air void content, capillary porosity, and micro-cracks in the interlayer should be carried out in the future.
- Applying water mist on the substrate surface may prompt the formation of the portlandite and/or calcite layer in the interlayer zone. The interactive connection between two layers induced by C-S-H formation at the interface appeared to be inhibited. In addition, excess water droplets (remained at the interface) may increase the local w/c, leading to higher capillary porosity. This can further dilute

the matrix density in the interlayer zone, thereby reducing the local mechanical performance.

Declaration of Competing Interest

The authors declare that they have no known competing financial interests or personal relationships that could have appeared to influence the work reported in this paper.

Acknowledgments

Yu Chen and Ze Chang would like to acknowledge the funding supported by China Scholarship Council under grant No. 201807720005 and 201806060129, respectively. The authors also appreciate the initial investigation of Mr. Koen Jansen. In addition, the authors want to thank Mr. Arjan Thijssen and Mr. Maiko van Leeuwen for their supports in CT scanning, ESEM and uniaxial tensile test. Burgess Pigment Company is thanked for the supply of the Optipozz®Burgess metakaolin.

Appendix A

Fig. A1 shows water loss on the surface of samples with 4 h air curing, plastic film covering, and wet towel covering. The simulated stress and strain curves and fracture patterns of printed specimens with different curing methods (i.e., plastic film covering, wet towel covering, and water mist-30 min/-60 min) are presented in Figs. A2 and A3.

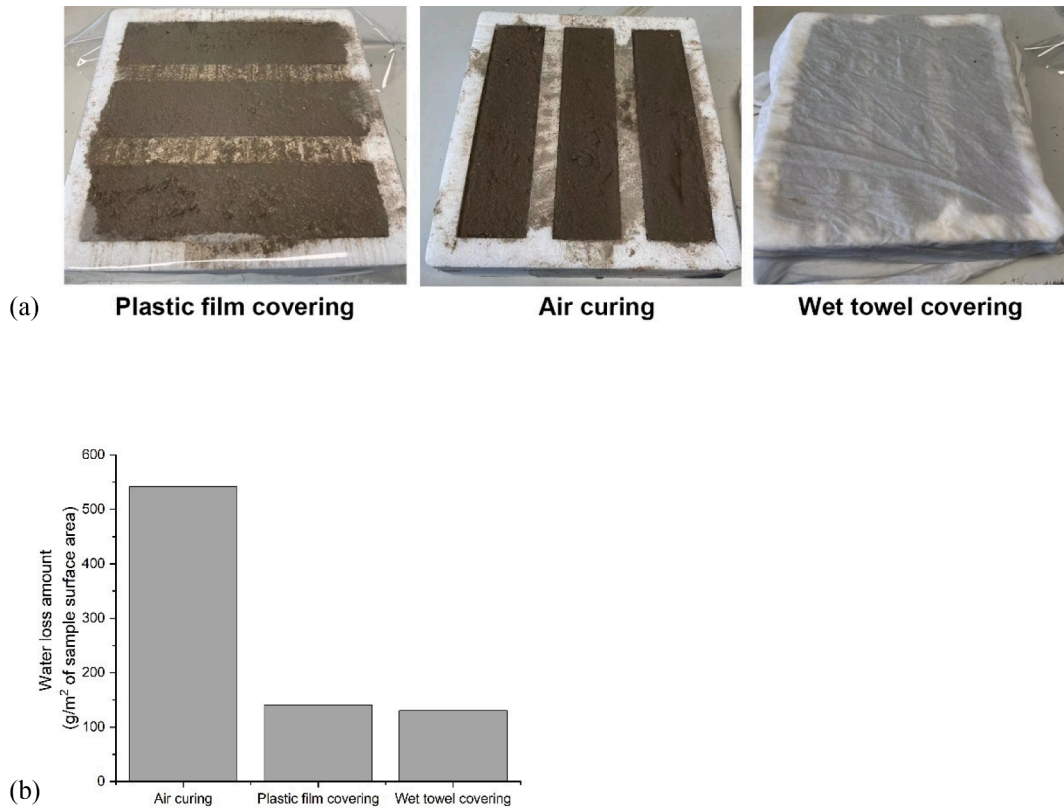


Fig. A1. (a) The fresh mixture was filled in the polystyrene prism mold. Only one surface was exposed to the ambient environment, or covered by the plastic film or wet towel. Thus, the mass loss after 4 h time interval can be regarded as the surface water evaporation of the fresh sample. (b) Water loss of samples with 4 h air curing, plastic film covering, and wet towel covering (water loss amount = (sample mass before 4 h – sample mass after 4 h)/sample surface area).

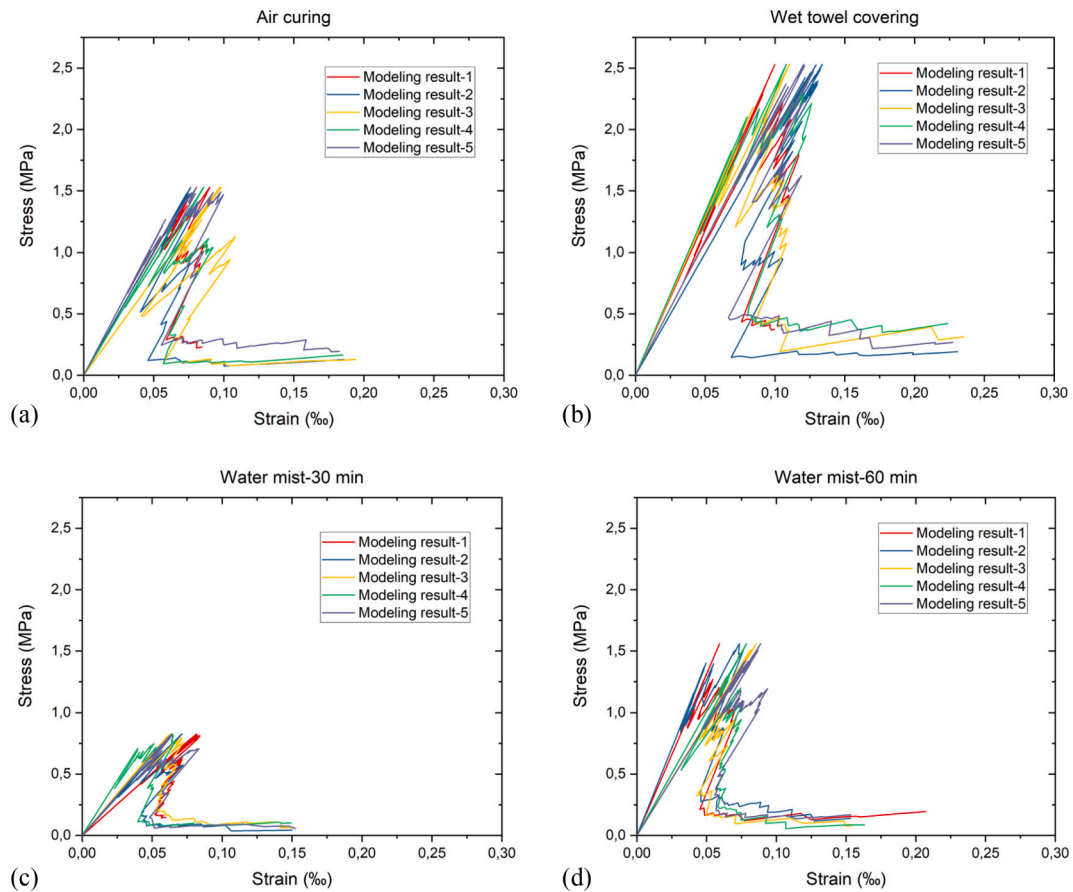


Fig. A2. The simulated stress and strain curves of printed specimen: (a) Air curing; (b) Wet towel covering; (c) Water mist-30 min; (d) Water mist-60 min.

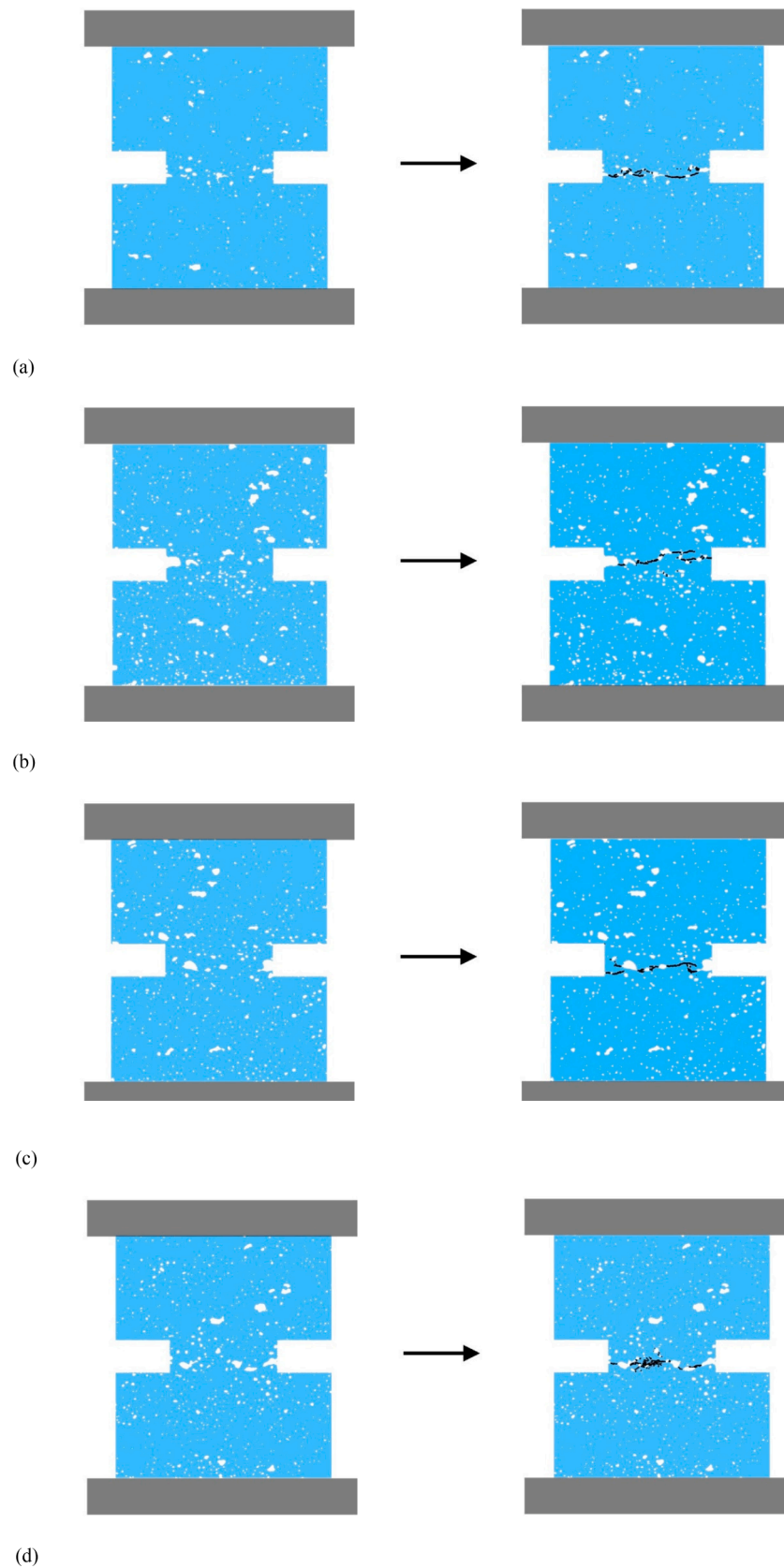


Fig. A3. The simulated crack patterns of printed specimen at fracture stage (left: initial specimen; right: fractured specimen): (a) Air curing; (b) Wet towel covering; (c) Water mist-30 min; (d) Water mist-60 min. White area-air voids; Black area-cracks; Blue area-cementitious materials.

References

- [1] A. Perrot, A. Pierre, V.N. Nerella, R.J.M. Wolfs, E. Keita, S.A.O. Nair, N. Neithalath, N. Roussel, V. Mechtcherine, From analytical methods to numerical simulations: A process engineering toolbox for 3D concrete printing, *Cem. Concr. Compos.* 122 (2021) 104164, <https://doi.org/10.1016/j.cemconcomp.2021.104164>.
- [2] J.G. Sanjayan, R. Jayatilakage, P. Rajeev, Vibration induced active rheology control for 3D concrete printing, *Cem. Concr. Res.* 140 (2021) 106293, <https://doi.org/10.1016/j.cemconres.2020.106293>.
- [3] M.K. Mohan, A.V. Rahul, K. Van Tittelboom, G. De Schutter, Rheological and pumping behaviour of 3D printable cementitious materials with varying aggregate content, *Cem. Concr. Res.* 139 (2021) 106258, <https://doi.org/10.1016/j.cemconres.2020.106258>.
- [4] G. De Schutter, K. Lesage, V. Mechtcherine, V.N. Nerella, G. Habert, I. Agusti-Juan, Vision of 3D printing with concrete — Technical, economic and environmental potentials, *Cem. Concr. Res.* 112 (2018) 25–36, <https://doi.org/10.1016/j.cemconres.2018.06.001>.
- [5] B. Zhu, J. Pan, Z. Zhou, J. Cai, Mechanical properties of engineered cementitious composites beams fabricated by extrusion-based 3D printing, *Eng. Struct.* 238 (2021) 112201, <https://doi.org/10.1016/j.engstruct.2021.112201>.
- [6] R.A. Buswell, W.R. Leal de Silva, S.Z. Jones, J. Dirrenberger, 3D printing using concrete extrusion: A roadmap for research, *Cem. Concr. Res.* 112 (2018) 37–49, <https://doi.org/10.1016/j.cemconres.2018.05.006>.
- [7] B. Zhu, B. Nematollahi, J. Pan, Y. Zhang, Z. Zhou, Y. Zhang, 3D concrete printing of permanent formwork for concrete column construction, *Cem. Concr. Compos.* 121 (2021) 104039, <https://doi.org/10.1016/j.cemconcomp.2021.104039>.
- [8] C. Zhang, V. Naidu, A. Krishna, S. Wang, Y. Zhang, V. Mechtcherine, N. Banthia, Mix design concepts for 3D printable concrete: A review, *Cem. Concr. Compos.* 122 (2021), 104155, <https://doi.org/10.1016/j.cemconcomp.2021.104155>.
- [9] Y. Chen, S. He, Y. Gan, O. Çopuroğlu, F. Veer, E. Schlangen, A review of printing strategies, sustainable cementitious materials and characterization methods in the context of extrusion-based 3D concrete printing, *J. Build. Eng.* 45 (2022) 103599, <https://doi.org/10.1016/j.jobte.2021.103599>.
- [10] V.C. Li, F.P. Bos, K. Yu, W. McGee, T.Y. Ng, S.C. Figueiredo, K. Nefs, V. Mechtcherine, V.N. Nerella, J. Pan, G.P.A.G. van Zijl, P.J. Kruger, On the emergence of 3D printable Engineered, Strain Hardening Cementitious Composites (ECC/SHCC), *Cem. Concr. Res.* 132 (2020) 106038, <https://doi.org/10.1016/j.cemconres.2020.106038>.
- [11] Y. Chen, S. Chaves Figueiredo, Z. Li, Z.e. Chang, K. Jansen, O. Çopuroğlu, E. Schlangen, Improving printability of limestone-calcined clay-based cementitious materials by using viscosity-modifying admixture, *Cem. Concr. Res.* 132 (2020) 106040, <https://doi.org/10.1016/j.cemconres.2020.106040>.
- [12] Y. Chen, F. Veer, O. Copuroglu, *A Critical Review of 3D Concrete Printing as a Low CO2 Concrete Approach*, *Heron.* 62 (2017) 167.
- [13] G. Ma, N.M. Salman, L.i. Wang, F. Wang, A novel additive mortar leveraging internal curing for enhancing interlayer bonding of cementitious composite for 3D printing A novel additive mortar leveraging internal curing for enhancing interlayer bonding of cementitious composite for 3D printing, *Constr. Build. Mater.* 244 (2020) 118305, <https://doi.org/10.1016/j.conbuildmat.2020.118305>.
- [14] S. Bhattacherjee, A.S. Basavaraj, A.V. Rahul, M. Santhanam, R. Gettu, B. Panda, E. Schlangen, Y. Chen, O. Copuroglu, G. Ma, L.i. Wang, M.A. Basit Beigh, V. Mechtcherine, Sustainable materials for 3D concrete printing, *Cem. Concr. Compos.* 122 (2021) 104156, <https://doi.org/10.1016/j.cemconcomp.2021.104156>.
- [15] Y. Chen, S. He, Y. Zhang, Z. Wan, O. Çopuroğlu, E. Schlangen, 3D printing of calcined clay-limestone-based cementitious materials, *Cem. Concr. Res.* 149 (2021) 106553, <https://doi.org/10.1016/j.cemconres.2021.106553>.
- [16] F. Boscaro, E. Quadranti, T. Wangler, S. Mantellato, L. Reiter, R.J. Flatt, Eco-Friendly, Set-on-Demand Digital Concrete, 3D Print, *Addit. Manuf.* 9 (1) (2022) 3–11, <https://doi.org/10.1089/3dp.2020.0350>.
- [17] T. Ding, J. Xiao, S. Zou, Y.u. Wang, Hardened properties of layered 3D printed concrete with recycled sand, *Cem. Concr. Compos.* 113 (2020) 103724, <https://doi.org/10.1016/j.cemconcomp.2020.103724>.
- [18] G. Bai, L.i. Wang, G. Ma, J. Sanjayan, M. Bai, 3D printing eco-friendly concrete containing under-utilised and waste solids as aggregates, *Cem. Concr. Compos.* 120 (2021) 104037, <https://doi.org/10.1016/j.cemconcomp.2021.104037>.
- [19] A.V. Rahul, M.K. Mohan, G. De Schutter, K. Van Tittelboom, 3D printable concrete with natural and recycled coarse aggregates: Rheological, mechanical and shrinkage behaviour, *Cem. Concr. Compos.* 125 (2022) 104311, <https://doi.org/10.1016/j.cemconcomp.2021.104311>.
- [20] Y. Chen, K. Jansen, H. Zhang, C. Romero Rodriguez, Y. Gan, O. Çopuroğlu, E. Schlangen, Effect of printing parameters on interlayer bond strength of 3D printed limestone-calcined clay-based cementitious materials: An experimental and numerical study, *Constr. Build. Mater.* 262 (2020) 120094, <https://doi.org/10.1016/j.conbuildmat.2020.120094>.
- [21] N. Roussel, Rheological requirements for printable concretes, *Cem. Concr. Res.* 112 (2018) 76–85, <https://doi.org/10.1016/j.cemconres.2018.04.005>.
- [22] Y.W.D. Tay, G.H.A. Ting, Y.e. Qian, B. Panda, L. He, M.J. Tan, Time gap effect on bond strength of 3D-printed concrete, *Virtual Phys. Prototyp.* 14 (1) (2019) 104–113, <https://doi.org/10.1080/17452759.2018.1500420>.
- [23] Y. Weng, M. Li, D. Zhang, M.J. Tan, S. Qian, Investigation of interlayer adhesion of 3D printable cementitious material from the aspect of printing process, *Cem. Concr. Res.* 143 (2021) 106386, <https://doi.org/10.1016/j.cemconres.2021.106386>.
- [24] B. Panda, N.A.N. Mohamed, S.C. Paul, G.V.P.B. Singh, M.J. Tan, B. Šavija, The effect of material fresh properties and process parameters on buildability and interlayer adhesion of 3D printed concrete, *Materials (Basel).* 12 (2019) 2149, <https://doi.org/10.3390/ma12132149>.
- [25] R.J.M. Wolfs, F.P. Bos, T.A.M. Sallet, Hardened properties of 3D printed concrete: The influence of process parameters on interlayer adhesion, *Cem. Concr. Res.* 119 (2019) 132–140, <https://doi.org/10.1016/j.cemconres.2019.02.017>.
- [26] B. Panda, S.C. Paul, N.A.N. Mohamed, Y.W.D. Tay, M.J. Tan, Measurement of tensile bond strength of 3D printed geopolymer mortar, *Meas. J. Int. Meas. Confed.* 113 (2018) 108–116, <https://doi.org/10.1016/j.measurement.2017.08.051>.
- [27] Z. Geng, W. She, W. Zuo, K. Lyu, H. Pan, Y. Zhang, C. Miao, Layer-interface properties in 3D printed concrete: Dual hierarchical structure and micromechanical characterization, *Cem. Concr. Res.* 138 (2020), 106220, <https://doi.org/10.1016/j.cemconres.2020.106220>.
- [28] Y. Xu, Q. Yuan, Z. Li, C. Shi, Q. Wu, Y. Huang, Correlation of interlayer properties and rheological behaviors of 3DPC with various printing time intervals, *Addit. Manuf.* 47 (2021) 102327, <https://doi.org/10.1016/j.addma.2021.102327>.
- [29] J. Kruger, A. du Plessis, G. van Zijl, An investigation into the porosity of extrusion-based 3D printed concrete, *Addit. Manuf.* 37 (2021) 101740, <https://doi.org/10.1016/j.addma.2020.101740>.
- [30] T.T. Le, S.A. Austin, S. Lim, R.A. Buswell, R. Law, A.G.F. Gibb, T. Thorpe, Hardened properties of high-performance printing concrete, *Cem. Concr. Res.* 42 (3) (2012) 558–566, <https://doi.org/10.1016/j.cemconres.2011.12.003>.
- [31] E. Keita, H. Bessaies-Bey, W. Zuo, P. Belin, N. Roussel, Weak bond strength between successive layers in extrusion-based additive manufacturing: measurement and physical origin, *Cem. Concr. Res.* 123 (2019) 105787, <https://doi.org/10.1016/j.cemconres.2019.105787>.
- [32] D. Marchon, S. Kawashima, H. Bessaies-Bey, S. Mantellato, S. Ng, Hydration and rheology control of concrete for digital fabrication: Potential admixtures and cement chemistry, *Cem. Concr. Res.* 112 (2018) 96–110, <https://doi.org/10.1016/j.cemconres.2018.05.014>.
- [33] Y. Chen, O. Çopuroğlu, C. Romero Rodriguez, F.F.d. Mendonca Filho, E. Schlangen, Characterization of air-void systems in 3D printed cementitious materials using optical image scanning and X-ray computed tomography, *Mater. Charact.* 173 (2021) 110948, <https://doi.org/10.1016/j.matchar.2021.110948>.
- [34] H. Lee, J.-H.-J. Kim, J.-H. Moon, W.-W. Kim, E.-A. Seo, Correlation between pore characteristics and tensile bond strength of additive manufactured mortar using X-ray computed tomography, *Constr. Build. Mater.* 226 (2019) 712–720, <https://doi.org/10.1016/j.conbuildmat.2019.07.161>.
- [35] J. Van Der Putten, M. Deprez, V. Cnudde, G. De Schutter, K. Van Tittelboom, Microstructural Characterization of 3D Printed Cementitious Materials, *Materials (Basel).* 12 (2019) 2993, <https://doi.org/10.3390/ma12182993>.
- [36] S. Yu, M. Xia, J. Sanjayan, L. Yang, J. Xiao, H. Du, Microstructural characterization of 3D printed concrete, *J. Build. Eng.* 44 (2021) 102948, <https://doi.org/10.1016/j.jobte.2021.102948>.
- [37] J. Liu, S. Li, C. Gunasekara, K. Fox, P. Tran, 3D-printed concrete with recycled glass: Effect of glass gradation on flexural strength and microstructure, *Constr. Build. Mater.* 314 (2022) 125561, <https://doi.org/10.1016/j.conbuildmat.2021.125561>.
- [38] H. Zhang, B. Šavija, S.C. Figueiredo, E. Schlangen, Experimentally validated multi-scale modelling scheme of deformation and fracture of cement paste, *Cem. Concr. Res.* 102 (2017) 175–186, <https://doi.org/10.1016/j.cemconres.2017.09.011>.
- [39] E. Schlangen, *Experimental and Numerical Analysis of Fracture Processes in Concrete*, Delft University of Technology, 1993.
- [40] Z. Chang, H. Zhang, E. Schlangen, B. Šavija, Lattice fracture model for concrete fracture revisited: Calibration and validation, *Appl. Sci.* 10 (14) (2020) 4822, <https://doi.org/10.3390/app10144822>.
- [41] Y. Chen, C. Romero Rodriguez, Z. Li, B. Chen, O. Çopuroğlu, E. Schlangen, Effect of different grade levels of calcined clays on fresh and hardened properties of ternary-blended cementitious materials for 3D printing, *Cem. Concr. Compos.* 114 (2020) 103708, <https://doi.org/10.1016/j.cemconcomp.2020.103708>.
- [42] H. Zhang, B. Šavija, S. Chaves Figueiredo, M. Lukovic, E. Schlangen, Microscale testing and modelling of cement paste as basis for multi-scale modelling, *Materials (Basel).* 9 (11) (2016) 907, <https://doi.org/10.3390/ma9110907>.
- [43] H. Zhang, Y. Xu, Y. Gan, Z.e. Chang, E. Schlangen, B. Šavija, Combined experimental and numerical study of uniaxial compression failure of hardened cement paste at micrometre length scale, *Cem. Concr. Res.* 126 (2019) 105925, <https://doi.org/10.1016/j.cemconres.2019.105925>.
- [44] Z. Chang, Y. Xu, Y. Chen, Y. Gan, E. Schlangen, B. Šavija, A discrete lattice model for assessment of buildability performance of 3D-printed concrete, *Comput. Civ. Infrastruct. Eng.* 36 (5) (2021) 638–655, <https://doi.org/10.1111/micc:v36.510.1111/micc:12700>.
- [45] E. Schlangen, E.J. Garboczi, Fracture simulations of concrete using lattice models: computational aspects, *Eng. Fract. Mech.* 57 (2-3) (1997) 319–332, [https://doi.org/10.1016/S0013-7944\(97\)00010-6](https://doi.org/10.1016/S0013-7944(97)00010-6).
- [46] H. Zhang, B. Šavija, M. Luković, E. Schlangen, Experimentally informed micromechanical modelling of cement paste: An approach coupling X-ray computed tomography and statistical nanoindentation, *Compos. Part B Eng.* 157 (2019) 109–122, <https://doi.org/10.1016/j.compositesb.2018.08.102>.
- [47] K. Mehta, P.J.M. Monteiro, *Microstructure and properties of hardened concrete*, in: *Concr. Microstruct. Prop. Mater.*, 3rd ed., McGraw-Hill, New York, 2016, pp. 41–80.
- [48] J.G. Sanjayan, B. Nematollahi, M. Xia, T. Marchment, Effect of surface moisture on inter-layer strength of 3D printed concrete, *Constr. Build. Mater.* 172 (2018) 468–475, <https://doi.org/10.1016/j.conbuildmat.2018.03.232>.
- [49] M. Lukovic, G. Ye, Effect of moisture exchange on interface formation in the repair system studied by X-ray absorption, *Materials (Basel).* 9 (1) (2016) 2, <https://doi.org/10.3390/ma9010002>.

- [50] M. Lukovic, Influence of Interface and Strain Hardening Cementitious Composite (SHCC) Properties on the Performance of Concrete Repairs, Delft University of Technology, 2016.
- [51] M. Palacios, R.J. Flatt, Working mechanism of viscosity-modifying admixtures, Elsevier Ltd (2015), <https://doi.org/10.1016/B978-0-08-100693-1.00020-5>.
- [52] W. Zuo, E. Keita, M. Bornert, N. Roussel, Drying of 3D Printed Mortar Filaments at Early Age Assessed by X-Ray Computed Tomography, Springer International Publishing (2020), https://doi.org/10.1007/978-3-030-49916-7_58.
- [53] V.N. Nerella, S. Hempel, V. Mechtcherine, Effects of layer-interface properties on mechanical performance of concrete elements produced by extrusion-based 3D-printing, Constr. Build. Mater. 205 (2019) 586–601, <https://doi.org/10.1016/j.conbuildmat.2019.01.235>.
- [54] N. De Belie, E. Gruyaert, A. Al-Tabbaa, P. Antonaci, C. Baera, D. Bajare, A. Darquennes, R. Davies, L. Ferrara, T. Jefferson, C. Litina, B. Miljevic, A. Otlewska, J. Ranogajec, M. Roig-Flores, K. Paine, P. Lukowski, P. Serna, J. M. Tulliani, S. Vucetic, J. Wang, H.M. Jonkers, A Review of Self-Healing Concrete for Damage Management of Structures, Adv. Mater. Interfaces. 5 (2018) 1–28, <https://doi.org/10.1002/admi.201800074>.
- [55] S. Chaves Figueiredo, O. Çopuroğlu, E. Schlangen, Effect of viscosity modifier admixture on Portland cement paste hydration and microstructure, Constr. Build. Mater. 212 (2019) 818–840, <https://doi.org/10.1016/j.conbuildmat.2019.04.020>.
- [56] O. Çopuroğlu, Revealing the dark side of portlandite clusters in cement paste by circular polarization microscopy, Materials (Basel). 9 (3) (2016) 176, <https://doi.org/10.3390/ma9030176>.